December 2018

Summertime Connecticut River Water Pathways and Wind Impacts

Yan Jia
Department of Marine Sciences, University of Connecticut, yan.jia@uconn.edu

Michael M. Whitney
Department of Marine Sciences, University of Connecticut, Michael.Whitney@uconn.edu

Summertime Connecticut River Water Pathways and Wind Impacts

Yan Jia[1*] and Michael M. Whitney[1]

[1]Department of Marine Sciences, University of Connecticut, 1080 Shennecossett Rd., Groton, CT, 06340.

*Corresponding author: Yan Jia (yan.jia@uconn.edu)

Key Points:

- Summer Connecticut River water has two main pathways: up-estuary entrained with dense water near-bottom; down-estuary near the surface.
- Drifter observations confirm the surface outflow pathway in Long Island Sound.
- Mild winds alter position and strength of the bottom inflow; and highly impact the estuarine water distribution on the continental shelf.

Abstract

Long Island Sound is a large macrotidal estuary. Connecticut River as the primary freshwater source enters near the sound's mouth. The summertime pathways of river water under low discharge and mild wind conditions are studied through both numerical simulations with a passive dye pulse and field surface drifter observations. Within the 19-day modeling analysis period, a third of the river dye pulse moves up-estuary with the near-bottom dense inflow into central and western sound with a spring-neap tidal modulation; another third leaves the sound with the near-surface outflow towards the continental shelf through Block Island Sound. The latter pathway is confirmed by field surface drifter tracks. Three scenarios of wind forcing are tested: a WRF-ROMS Coupled case, a NARR data forcing case, and a No-Wind case. The results show though the sound is tidal mixing dominated, mild winds still alter the position and strength of the estuarine exchange either enhanced by the cross-estuary winds or through lateral straining. On the shelf, winds play a more important role on the fresher estuarine water distribution. The sensitivities of circulation, salinity, and numerical drifter tracks to different atmospheric forcings also are studied. The results suggest that the coupled model has better performance to simulate surface drifter tracks.

Plain Language Summary

Connecticut River is the primary freshwater source to Long Island Sound. It enters near the sound mouth, where dense continental shelf water intrudes in. The aims are to find out where the summer river waters go and what drives it. In particular, the mild wind impacts on the river water distributions are studied. Simulations with a river water dye pulse show two main pathways simultaneously: in 19 days, a third of the river water moves toward the sound head with a near-bottom dense inflow; another third of the river water leaves through the sound mouth at the surface and later on enters onto the shelf. The latter pathway is confirmed by field surface drifter tracks. Three scenarios of wind forcing are tested: a spatial varied wind case, a relatively spatial uniform wind case, and a no wind case. The results show winds speedup the up-estuary transport of the river water in central sound. On the continental shelf, winds play a more important role on the estuarine outflow distribution. Results suggest the spatial varied wind model has better performance on modeling surface drifter tracks. This study gives a clear picture on the summertime Connecticut River water pathways and the related dynamics.

Index Terms and Keywords

4235 Estuarine processes, 4219 Continental shelf and slope processes, 4534 Hydrodynamic modeling, 4536 Hydrography and tracers, 3339 Ocean/atmosphere interactions

Connecticut River, freshwater pathway, dye, drifter, ROMS, WRF

1 Introduction

Riverine freshwater inflows, tides, and winds control estuarine circulation. Typically, riverine freshwater generates vertical and horizontal density gradients such that density increases with depth and towards the estuary mouth. The combination of this buoyancy and tidal mixing often leads to a two-layer gravitational flow with surface outflow of fresher water and bottom inflow of saline water (Geyer & MacCready, 2014). In wider estuaries or with cross-estuary bathymetry variations, the outflow and inflow layers can be laterally (as well as vertically) offset

from each other (e.g. Valle-Levinson et al., 2003; Whitney et al., 2016). Such exchange flow can adjust with spring-neap tidal variations (Ribeiro et al., 2004).

The Connecticut River flows into the Long Island Sound (LIS), a large (160 km length) and wide (30 km maximum width) macrotidal estuary on the northeast U.S. coast. The sound is resonant to semi-diurnal lunar (M_2) tides due to its length and bathymetry (20 m average depth) (Wong, 1991). The Connecticut River enters near the sound mouth where tidal currents are strong (~1 ms^{-1}) and contributes approximately 72% of riverine inflow to the sound (Koppelman et al., 1976). Having the primary river entering closer to the estuarine mouth than the head is a major departure from most other estuaries. The positioning of the riverine inflow may create a residual flow field with distinct differences from the classic two-layer gravitational estuarine flow pattern.

During summertime the Connecticut River discharge (Figure 2) is lower than average (550 m^3s^{-1}). Garvine (1975) observed the summer river plume bulge is only 4 km offshore. Tidal motion exerts a strong influence on the plume nearfield salinity distribution. Yet recent studies (Codiga & Aurin, 2007; Whitney et al., 2016) with both observations and numerical methods indicate the upper-layer fresher outflow through eastern LIS is centered to the south (on the opposite side from the Connecticut River mouth) and the lower-layer saline inflow is centered to the north. Links between the river plume and the estuarine exchange flow need to be further studied.

Wind-driven circulation in large lakes and estuaries with homogenous density are well studied analytically (Csanady, 1973; Winant, 2004). The general flow pattern is downwind in shallow water and upwind in deep water. Winds also play important roles on modifying density structure. Strong winds, such as winter storms (e.g. Goodrich et al., 1987; Whitney & Codiga, 2011) and hurricanes (Li et al., 2007), can decrease/break stratification by enhancing vertical mixing; while moderate winds increase stratification by straining along-estuary density gradient (Scully et al., 2005).

LIS is wide enough that winds impact can be important in both along- and cross-estuary directions. Whitney and Codiga (2011) found strong along-estuary wind events cause more laterally aligned flows, especially during down-estuary wind events (winter dominant winds over LIS). In summer, winds are weaker, but can have significant spatial variations. Observations and model simulations found summer sea breezes develop along the shorelines of LIS (Sinsky, 2016). However, the role of moderate winds on freshwater distribution and estuarine exchange flow in LIS is still unclear.

Regional atmospheric models are well suited to force various real-time models in Mid-Atlantic Bight (Wilkin & Hunter, 2013). However, those 10-30 km resolution models may underestimate wind impacts on estuarine circulation (Scully, 2010; Xie & Li, 2018) and cause errors on predicting surface drifter trajectories (Cucco et al., 2016). Especially, when estuaries are at similar or smaller scales to the forcing resolution. Consequently, observed wind fields or higher resolution modeled winds are needed. Furthermore, two-way coupling may be advantageous for representing wind influence.

There are three objectives of this study. First, detect summertime Connecticut River water pathways in LIS and its ambient water. Second, describe influences of moderate winds on freshwater distribution and estuarine exchange flow. Third, characterize the sensitivity of river water pathways to the treatment of wind forcing (i.e., coupled high-resolution model vs. low-

resolution reanalysis product). The following sections describe methods, results, discussion, and conclusions.

2 Methods

2.1 Model configuration

The Regional Ocean Modeling System (ROMS) is applied to simulate conditions in LIS and the adjacent waters. ROMS is a free-surface, terrain-following (S-coordinates, Song & Haidvogel, 1994), primitive-equation ocean circulation model solving the nonlinear momentum, mass, and tracer conservation equations under hydrostatic and Boussinesq approximations (Haidvogel et al., 2000). Horizontal momentum advection is approximated with a third-order upstream biased and a fourth-order centered scheme for 3D and 2D (vertically-integrated) equations, respectively. A fourth-order centered scheme is applied for vertical advection. These options represent the current default settings in ROMS. A 3rd High-order Spatial Interpolation at the Middle Temporal level (HSIMT; Wu & Zhu, 2010) advection scheme is applied to tracer equations for this study. The generic length scale (GLS) method k-epsilon closure scheme is used for the parameterization of vertical turbulent viscosity and diffusivity. Quadratic bottom friction is prescribed with the bottom drag coefficient of 3×10^{-3} in most areas. The bottom drag coefficient is enlarged to 5 times in eastern LIS (ELIS) and the adjacent west half of Block Island Sound (BIS) for depths 20 to 85 m in order to obtain better water level simulation results compared to NOAA tidal station data in LIS (New London, New Haven, Bridgeport, CT & Kings Point, NY) and better tidal current results compared to observed depth-averaged M_2 tidal currents (Bennett et al., 2010). A similar drag coefficient increase is used in Whitney and Codiga (2011).

The model domain includes the entire LIS and covers its surrounding shelf regions extending from Cape Cod to New Jersey (Figure 1). Both the *x*- and *y*-directions are 9.5º counterclockwise from the east and north, respectively. Note that the model domain and settings are not the same as used in Whitney et al. (2016), though they share many similarities. The horizontal resolution varies from 500 m to 2 km, with the finest resolution inside LIS. Vertically there are 30 sigma layers that are evenly distributed throughout the water column. The bathymetry data is from the NOAA National Centers for Environment Information (NCEI) 3 arc-second U.S. Coastal Relief Model (CRM, http://www.ngdc.noaa.gov/mgg/coastal/crm.html). A low-pass filter with a 1 km radius is applied to the bathymetry data. Along the open boundaries, sea surface elevation and depth-averaged velocity have Chapman (1985) and Flather (1976) boundary conditions, respectively. These conditions are imposed with both subtidal ocean variables from the HYbird Coordinate Ocean Model (HYCOM) and eight semidiurnal and diurnal harmonic tidal constituents (M_2, S_2, N_2, K_2, K_1, O_1, P_1 & Q_1) supplied from the OSU TOPEX/Poseidon Global Inverse Solution TPXO (Egbert & Erofeeva, 2002). The Orlanski radiation boundary condition (Orlanski, 1976) is applied to 3D velocity and all tracers. According to tests, modeled salinity with original HYCOM forcing is saltier than a 4-yr observational record from Martha's Vineyard Coastal Observatory (http://www.whoi.edu/mvco/ocean-data) near the model's east boundary. And the wintertime HYCOM temperature is warmer than observations. Modifications are applied to HYCOM data to get better simulations matching with the observations: Salinity is reduced by 0.93 from year day 160 to 240; during other times, it is reduced by 0.6. And the maximum salinity is fixed to 34. Temperature is not modified from year day 71 to 200 but HYCOM data is reduced by 2 ^{o}C

141 during in the rest period. Velocity, temperature, and salinity are daily nudged to the modified
142 HYCOM data at the open boundaries.

143 Daily river discharge is supplied from U.S. Geological Survey (USGS) National Water
144 Information System (http://waterdata.usgs.gov/nwis) and is scaled up to include the ungauged
145 area. There are four major rivers including the Connecticut, Housatonic, Thames, and Hudson
146 Rivers, and 75 small rivers and non-river coastal watersheds. Two large wastewater treatment
147 outfalls with steady discharges of 31 and 15 m^3s^{-1} are added in East River, NY.

148 Three types of surface forcing are tested: 1. The "Coupled case" couples ROMS with
149 Weather Research and Forecasting Model (WRF) to provide atmospheric forcing with a high
150 degree of spatial variability. This process is done by applying the Coupled-Ocean-Atmosphere-
151 Wave-Sediment Transport Modeling System (COAWST, Warner et al., 2008, 2010). 2. "No-
152 Wind case" turns off the wind stress but keeps the surface heat fluxes and air pressure from WRF
153 as in the Coupled case. 3. The "NARR case" uses the 32-km resolution North America Regional
154 Reanalysis (NARR, Mesinger et al., 2006) data to force the model with relatively low spatial
155 variability.

156 For the Coupled case, WRF contains three domains (Figure 1). A 9-km horizontal
157 resolution large domain covers the northeast coast of U.S. Two nested domains are centered on
158 LIS, with 3-km and 1-km horizontal resolutions, respectively. There are 30 vertical layers in
159 WRF. Details of the WRF settings and modification to the NARR data near the coastal region
160 are included in Lombardo et al. (2016). WRF directly supplies shortwave radiation, longwave
161 radiation, latent heat flux, sensible heat flux, wind stress, and air pressure to ROMS. ROMS
162 updates sea surface temperature to WRF. The data exchanging interval is 0.5 hours. The WRF
163 model spins up for 24 hours before coupling with ROMS.

164 For the NARR case, ROMS applies bulk formulae (Fairall et al., 2003) to compute
165 surface fluxes of momentum, sensible, latent, and longwave heat. The surface winds, humidity,
166 air temperature, surface pressure, net shortwave radiation, and downward long wave radiation
167 are supplied from NARR. A 5-year (2011-2015) comparison of NARR surface air temperature to
168 the NOAA buoy data (http://www.ndbc.noaa.gov) in LIS (Figure 1, marked as white triangles)
169 shows that NARR typically underestimates the wintertime air temperature. By filling gaps from
170 nearby buoys, a group of 5-year time series of buoy air temperature data is obtained. Then signal
171 periods shorter than 20 days are filtered by using a fast Fourier transform, to obtain reconstructed
172 air temperature data. The observation-based air temperature time series are used to replace the
173 original NARR air temperature over water.

174 The three tests are initialized from a same long-term spin-up run which starts at January 1,
175 2011 forced by NARR data with other settings the same as described above. The spin-up run is
176 stabilized after two years. All cases run for 19 days starting on 21 August 2013, during spring
177 tides (Figure 2, top panel). The neap tides occur at the 16^{th} M_2 tidal cycle. The study period is
178 characterized by low discharge from the Connecticut River. The averaged river discharge is 250
179 m^3s^{-1} (Figure 2, second panel), which is half to the annual mean value.

180 The passive tracer computational capabilities of ROMS are used to track the Connecticut
181 River water. To accomplish this, a pulse of dye (a conservative passive tracer) is released at 12
182 km upstream from the river mouth, where the salinity is 0 throughout the water column. The dye
183 has a unit concentration and is released with a constant 10 m^3s^{-1} flux for one M_2 tidal cycle. It

takes about one day for the dye to reach the river mouth, by which time it has completely mixed through the Connecticut River freshwater.

2.2 Surface drifters

Six CODE/DAVIS type satellite-tracked surface drifters were deployed in the Connecticut River plume near the river mouth from R/V Lowell Weicker. Releasing started two hours before the daytime high tide, with a ~1-hour interval, on 21 August 2013. The drifter floats within the top 1-m water and reports position every half hour. Three drifters reported useful positions longer than 17 days. The longest one lasted for 28 days. The low-cost hand-built drifters were designed by J. P. Manning at NOAA National Marine Fisheries Service (www.nefsc.noaa.gov/drifter/).

In order to evaluate the drifter track's sensitivity to various wind forcing, six 1-m isobaric numerical drifters are released in each of the three model runs at the same times and locations as the field drifters. Furthermore, a cluster of 275 1-m deep isobaric numerical drifters is released from 11 grid cells at the river mouth to obtain statistical information on drifter tracks They are released with half hour interval during the field operational tidal cycle.

2.3 LIS survey data

The Connecticut Department of Energy and Environmental Protection (CT-DEEP) conducted a regular survey in LIS during 27~29 August 2013. Comparison of salinity and temperature along the sound's channel show, for all three cases, the root-mean-square-error (RMSE) of salinity and temperature is ~0.44 and ~2.2 °C, respectively. Both RMSE are largely due to bias at this period. The model results are saltier and warmer than observations. However, the salinity and temperature gradient structures are well captured by the models. Deignan-Schmidt and Whitney (2017) reported, compared to CT-DEEP, RMSE of salinity and temperature are 0.89 and 2.28 °C, respectively, during summer 2013 with a model setup of similar to Whitney and Codiga (2011).

3 Results

3.1 Summertime winds over LIS

There are conspicuous differences in the wind forcing among runs, therefore it is important to first compare model winds with observations in LIS. The time mean of spatial averaged wind speeds are 4.9, 4.3, and 3.9 ms^{-1} for WRF, NARR, and buoy data, respectively. Overall, winds during the modeling period are mild. The squared correlation coefficients for the spatial averaged WRF and NARR U-wind (along-estuary) with the buoy wind are 0.74 and 0.79, respectively; the corresponding values are 0.87 and 0.79 for the V-wind (cross-estuary). In general, both the WRF and NARR winds display similar synoptic weather time scale variations to the buoy data (Figure 2), but also have obvious differences on individual wind events.

3.2 Summertime hydrographic patterns in LIS and its ambient water

The Connecticut River significantly impacts the salinity field in ELIS. Observations show during high discharge the river front extends more than 10 km toward the sound mouth at low slack water (Garvine, 1974); while the low discharged river plume is only 4 km offshore (Garvine, 1975). Time averaged results show (Figure 3) the Connecticut River plume only

spreads 2 km offshore at the surface and spreads farther westward than eastward. A salt tongue extends from the sound mouth into central LIS (CLIS). Such intrusion is more pronounced at the bottom. It fills the isobaths bounding the deepest areas west of the Mattituck Sill. Correspondingly in LIS, bottom flow moves up-estuary westward and surface flow moves down-estuary. This aspect of the sound's circulation is consistent with the typical two-layer estuarine exchange flow pattern. On the shelf, the fresher estuarine surface outflow propagates down the Long Island coast.

3.3 Summertime Connecticut River water pathways

The progression of Connecticut River waters is revealed by tracking a simulated dye (or passive tracer) pulse originating from the river. Dye distribution progressions are examined using the tidal averaged water-column maximum dye concentrations (Figure 4, top row). For the Coupled case, after 11 tidal cycles, the higher concentration dye (hereafter named "dye core") is mostly in ELIS, especially around the river mouth. The eastern edge of the dye has passed through BIS and reaches the shelf; while the western edge just slowly extends over the Mattituck Sill. At the 19th tidal cycle, three tidal cycles after the neap tide, the dye core moves over the sill. After 36 tidal cycles, it has spread along the deep channel in CLIS and WLIS, with a branch attaching to the north shore. Such dye distribution pattern reveals the preferred up-estuary pathways of the Connecticut River water. In BIS and on the shelf, though the concentration is much lower than in the up-estuary areas, the dye spreads faster down- and cross-shelf. At the end, the dye core area is order magnitude smaller than the total dye spreading.

The distribution of Connecticut River water is further studied with along-estuary section views of dye concentration and salinity (Figure 5, top row). At the 11th tidal cycle, the maximum dye concentration in the Coupled case is at the surface of S5 (the nearest section grid to the river mouth). Stratification occurs at 10-m shallower in the dye core region. The dye's western edge reaches the Mattituck Sill. While the 29-isohaline locates east of the sill. After the neap tides, at the 19th tidal cycle, the strongest stratification in ELIS is established, which extends deeper than 20 m. Meanwhile, both the dye core and the 29-isohaline has passed the sill along the bottom. At the end, the bottom intruding dye reaches the boundary of WLIS and CLIS. And the arriving of the 29-isohaline enhances stratification in CLIS. At the down-estuary side, the dye is well diluted vertically.

Analyzing time series of dye storage adds quantitative details on the dye spread (Figure 6). For the Coupled case, before the neap tide (the 16th tidal cycle), total dye storage in ELIS decreases slowly; but the dye storage 10-m below keeps increasing and exceeds 50%. Between the 20th and 25th tidal cycle, 28% dye quickly leaves ELIS. Among that nearly 20% moves into CLIS primarily through the lower layer. The dye storage in BIS also peaks during this period. The total storage peaks near 30% in CLIS and starts dropping after the dye entering WLIS. Finally, about 5% of the dye enters WLIS, mainly through bottom. After 36th tidal cycles, the dye is about equally stored in ELIS, up-estuary in CLIS and WLIS, and down-estuary in BIS and the shelf. The up-estuary transport is largely associated with the timing of the spring-neap tides.

In order to detect the Connecticut River water surface pathways, six satellite-tracked surface observational drifters were deployed on 21 August 2013 inside the river plume near its mouth (Figure 7, upper left). All drifters reached the sound mouth within three tidal cycles. One (black) was captured by a boat. The rest drifted into BIS through the southwest corner of Fishers Island after three days. Three tidal cycles later, one grounded at Fishers Island due to south

winds. Three of the remaining four went southward across BIS in day 6, 7, and 8, respectively. Then they moved downshelf with the estuarine buoyant outflow. One took three weeks first circling around Block Island clockwise then moved farther cross-shelf.

In the Coupled case, six 1-m isobaric simulated drifters are released at the same times and locations as the field drifters to conduct one-on-one comparison (Figure 7, upper right). All six drifters reached the sound mouth in three to four tidal cycles and entered BIS after 2.5 days. Later on, the simulated drifter tracks capture both the southern cross-sound and the northern circle-island routes. Both the field and modeled drifter tracks reveal the surface down-estuary pathways of Connecticut River water during summertime low discharge condition.

3.4 Roles of winds

3.4.1 Impacts on river water pathways

Compared to the Coupled case, eliminating wind stress alters the dye pulse distribution and the corresponding movement timing (Figure 4, middle row). After 11 tidal cycles, the No-Wind case dye travels slower in the down-estuary direction. However, eight tidal cycles later, its downshelf edge surpasses the Coupled one. At the end, the No-Wind case dye spreads more downshelf and less cross-shelf. In LIS, the dye core travels slower up-estuary but with higher concentration. That indicates the Coupled case has stronger bottom inflow. The along-estuary section views show (Figure 5, middle row) the up-estuary intrusion enters near-bottom after the neap tides. In addition, without wind stress, less dye is mixed into the upper layer in CLIS.

Before the neap tides, more No-Wind dye stays in ELIS and less moves to BIS compared to the Coupled case (Figure 6). However, the main difference occurs during the up-estuary transport stage. Although they both reach a final storage around 30% in CLIS, the No-Wind case dye increases at a slower rate; while the Coupled one increases sharply before reaching a relative steady storage. Less No-Wind case dye moves into WLIS. Despite these notable differences, the squared correlation coefficients of the dye distribution between cases is 0.61.

The one-on-one drifter track comparisons show (Figure 7, lower right) all the No-Wind drifters leave LIS. But their down-estuary tracks are more confined to the western BIS and later along the coast of Long Island.

To obtain more statistically meaningful intercomparison from the drifter simulations, a large drifter cluster is released from the Connecticut River mouth. Counting the number of drifters passing certain grid highlights the preferable drifter pathways for each case (Figure 8). Similar to the one-on-one comparison, all drifters in both the Coupled and No-Wind cases move down-estuary mainly past the southwest corner of the Fishers Island (through ‘the Race’). In BIS there is a southern route for drifter moving onto the shelf. Pathway differences are better displayed outside LIS. More Coupled case drifters circle around BIS and move farther cross-shelf; while over a hundred of the No-Wind case drifters travel the same downshelf route.

In general, mild westerly winds spread the river water farther offshore on the shelf at surface. In LIS, the presence of wind quickens the bottom up-estuary transport of the river water and also brings more bottom river water to the surface.

3.4.2 Impacts on salinity and circulation

The Coupled case standard deviation of salinity decreases from LIS to the shelf and decreases from surface to bottom (Table 1). The No-Wind case has similar patterns, with slightly higher surface values. The standard deviation of velocities show the Coupled case has more variations in *x*-direction than the No-Wind case both in LIS and on the shelf. The percentage of RMSE relative to the standard deviation of the Coupled case (Table 2) shows shutting down the wind causes a similar level of velocity alteration both in LIS and on the shelf. However, salinity is more impacted on the shelf. Especially at the surface, where the modification is nearly four times to that in LIS. Generally, winds have higher impact on the shelf salinity than in LIS.

Overall, comparisons of the dye pulse and salinity distributions between the Coupled and No-Wind cases indicate the summer wind forcing appreciably influence estuarine and particularly shelf dynamic structures, even though winds are mild.

3.5 Influence of wind resolution

3.5.1 Winds comparison

In LIS, both the WRF and NARR winds show similar level of temporal variations compared to the buoy data (Table 3). However, the WRF winds' spatial variation, like the buoy winds, is one order of magnitude higher than the NARR winds. In addition, multiregional statistics show the V-component (cross-estuary) of WRF winds has more spatial variation than its U-component (along-estuary), especially in LIS (Table 1).

3.5.2 Impacts on river water pathways

Dye pulse distribution differences between the NARR and Coupled cases show up after the neap tides (19^{th} tidal cycle, Figure 4 & 5 bottom rows). The up-estuary leading edge in the NARR case moves faster than the Coupled one. It is almost half way through CLIS. And its dye core has higher concentration. On the shelf, the dyed area in NARR case is larger and spreads farther offshore than the Coupled case. At the end of the analysis period, more NARR case dye moves into WLIS through the deep channel (Figure 5, between S2 & S3). By this time, the dye pattern on the shelf is differed from the Coupled one, which travels farther downshelf. The squared correlation coefficients of the dye distribution between cases is 0.81.

Compared to the Coupled case, the NARR case up-estuary dye transport starts right around the neap tide, occurring three tidal cycles earlier (Figure 6). Eventually, 4% more dye is transported into CLIS. However, the overall patterns of dye transport are similar between the two cases. Both enters WLIS around the 27^{th} tidal cycle, which is five tidal cycles earlier than the No-Wind one.

NARR drifters from both the one-on-one comparison (Figure 7, lower left) and the drifter cluster (Figure 8, right) display more similarities on the downshelf tracks to the observations. But the one-on-one comparison does not capture the northern circle-island route. And compared to the Coupled case, the NARR drifter cluster is less dispersed on the shelf, especially during the downshelf transport.

3.5.3 Impacts on salinity and circulation

For the standard deviation comparison, the NARR case has identical values to the Coupled one, except a higher surface salinity and lower U velocities on the shelf (Table 1). The percentages of RMSE relative to the standard deviation of the Coupled case (Table 2) show the

velocity variations are in similar level in LIS and on the shelf, but surface salinity is more sensitive to wind variation on the shelf.

3.6 Momentum diagnostics of the estuarine exchange flow in CLIS

The dye pulse movement differences in CLIS indicate that the early stage of bottom intrusion (20^{th} ~25^{th} tidal cycle) is a key period to study differences in the exchange flow between cases. Along sect-C (Figure 9, left column), the bottom inflow and surface outflow are bounded by the pycnocline for all cases. The isohalines tilt up northward but with noticeable differences between cases. The Coupled case has the strongest exchange flow, ranging from -0.14 to 0.17 ms^{-1}; the NARR case is slightly weaker, but with a strong cross-estuary salinity gradient in the middle depth; while the No-Wind case is the weakest and is nearly half the Coupled case.

Tidal-averaged momentum analysis is used to further describe the conspicuous differences among cases that are evident in the estuarine exchange flow and salinity structure at section-C (Figure 9, left column). The cross-estuary component of the total pressure gradient term (Figure 9, center column) and along-estuary flow share similar patterns (particularly for the NARR and No-Wind cases), suggesting a geostrophic connection. The corresponding baroclinic term (Figure 9, right column) is chiefly related to the cross-estuary salinity gradient.

Momentum balances that are averaged over section-C analyzed (Figure 10) where the sign convention has all the terms on the right-hand side (consistent with ROMS diagnostics) balancing the time averaged local acceleration (that is negligible at this time). Due to the eastward narrowing of the sound, the along-estuary horizontal advection is a big term in all cases, suggesting tides always play important roles with or without wind.

For the No-Wind case, horizontal advection and Coriolis acceleration are balanced by pressure gradient force (PGF) and bottom stress. Note, this balance departs from the classic estuarine balance between pressure gradients and friction. The barotropic and baroclinic PGFs oppose each other with stronger along-estuary components.

Both the Coupled and NARR case have larger cross-estuary wind stress than the along-estuary stress (Table 4). And the presence of wind stress greatly alters the momentum balances from the No-Wind case. Mainly, the barotropic, baroclinic PGFs and Coriolis acceleration adjust accordingly. For the Coupled case, PGF is against the strong southwest wind stress. Compared to the No-Wind case, the along-estuary barotropic PGF is four times smaller; and the cross-estuary barotropic PGF switches direction. The latter pattern is similar to the typical wind-driven momentum balance (Csanady, 1973). Which implies the strengthened exchange flow may be wind-driven. In addition, strong wind mixing largely weakens the baroclinic PGF compared to the No-Wind case. With the impacts of the mild NARR winds, both the barotropic and baroclinic PGF turns from more along-estuary in the No-Wind case to more cross-estuary.

A common feature in all cases is the Coriolis acceleration partially opposes the PGF, especially for the NARR and No-Wind cases. This suggests a quasi-geostrophic balance. Garvine (1995) introduces the Kelvin number, ratio of the buoyant structure width to the baroclinic Rossby radius, to classify coastal buoyant flows. Here, the modeled exchange flow width is ~20 km and the baroclinic Rossby radius (c/f, c is internal wave phase speed, and f is Coriolis parameter) is ~5 km, the corresponding Kelvin number is 4. A Kelvin number greatly larger than 1 has quasi-geostrophic property in the cross-estuary direction. That matches the modeled

momentum diagnostics. Both the windy cases have stronger quasi-geostrophic balance in cross-estuary direction than the No-Wind case. Which implies they may have stronger along-estuary exchange flow.

Overall the diagnostics indicate two ways to intensify the exchange flow. One is via wind-driven circulation. The other is more indirect: winds enhance the cross-estuary density gradient, which then enlarges the corresponding quasi-geostrophic component of the exchange flow.

4 Discussion

4.1 Summertime estuarine circulation

Early drifter track studies (Gross & Bumpus, 1972; Paskausky & Murphy, 1976; Paskausky, 1977) indicate a two-layer density-driven exchange flow exists in ELIS. Vieira (2000), based on combined observations, pointed out a bottom inflow that moves through ELIS into CLIS. Current observation along an ELIS ferry transect (Codiga & Aurin, 2007) indicate a near-surface outflow skewed to the southern side and an inflow offset deeper and to the north side. Prior model results also show these features (e.g. Whitney and Codiga, 2011; Whitney et al., 2016). This study shows the laterally offset surface-intensified outflow and bottom-intensified inflow exchange pattern not only exists in ELIS but also extends to the whole LIS.

4.2 Summertime Connecticut River water pathways and spring-neap control

Entering near the estuary mouth, the Connecticut River water pathways interacts with the two-layer exchange flow. A surface branch goes down-estuary with the outflow, then travels down-shelf as a buoyant coastal current; and a bottom branch goes up-estuary with the saltier estuarine inflow. During the 19-day analysis period, about equally a third of dye pulse leaves ELIS in both directions. The surface outflow branch is highly diluted, while the bottom inflow branch travels as a slowly diluting core.

Mattituck Sill plays an important role on the dye pulse and river water distribution in ELIS and CLIS. First, strong tidal currents over the rough bottom mix the pulse to deep layer (Gordon & Pilbeam, 1975). Second, the topographic tidal residual circulation around the sill brings the pulse southward cross-estuary (Whitney et al., 2014).

The model results disclose that the up-estuary bottom intrusion is the key mechanism transporting the river water westward in summer. The inflow has lateral variations strengthened to the north, and has temporal variations controlled by the spring-neap tidal cycle. Previous surveys support these findings. Based on yearlong bottom current meter records, Gordon and Pilbeam (1975) reported bottom saline inflows enter CLIS through the north end of the Mattituck Sill, then flow west-southwestward along isobaths. They proposed the bottom inflow is the only way for Connecticut River water enters CLIS all year long. Here, the dye pulse pathways support the conclusion, at least for summertime.

Unlike the continuous down-estuary dye transport, the strong spring-neap control over the sill sends the dye up-estuary as pulse. With section observations, Valle-Levinson and Wilson (1994) found bottom dense water intrusion over the sill before neap tide and retreated seaward after spring tide during August 1987. Observations during summer 1990 on CT-DEEP station I2, which is on the dye pulse pathway in CLIS, show bottom water density experiences spring-neap

oscillation. Such spring-neap patterns are also discerned in WLIS (O'Donnell et al., 2008) and BIS (Liu et al., 2017). In contrast, without lateral density gradient and run only for five tidal cycles, Signell et al. (2000) simulated fairly uniform bottom inflow in CLIS besides the axial depression.

4.3 Wind impacts on estuary circulation and river water distribution

Summer winds over LIS are moderate (on average <5 ms^{-1}). In order to find out how important is the role of winds, three scenarios of wind forcing were tested. Both the Coupled and NARR case winds are slightly stronger than the buoy observations. The Coupled winds are the most energetic. All three cases exhibit the up- and down-estuary river water pathways and have a high degree of similarity. Nevertheless, different wind choices bring noticeable variations. For instances, the dye pulse distribution pattern on the shelf, the dye movement timing and strength in CLIS. The No-Wind case clearly illustrates moderate winds are still a necessary influence on the river water pathways and estuarine exchange flow.

Winds have two ways to influence the estuarine circulation: directly through wind-driven circulation and indirectly by altering density structures. The wind-driven circulation is first evaluated. The steady-state, non-rotational, linear barotropic wind-driven circulation along a rectangular channel cross section gives an estimate of the along-estuary velocity $u_w \sim \tau_x H/4\rho K$ (Chen & Sanford, 2009; Whitney & Codiga, 2011), where τ_x is the along-estuary wind stress (Table 4), *H* is 28 m of water depth, ρ is sea water density, *K* is eddy viscosity. For the Coupled and NARR case, the modeled *K* are 0.006 m^2s^{-1} and 0.004 m^2s^{-1}, respectively. The corresponding u_w are both 0.035 ms^{-1}.

Yet LIS is wide enough to consider the Coriolis impacts. Based on Winant (2004), a rotational solution estimation is $u_w \sim (a\tau_x - b\tau_y)H/\rho K$, where $\tau_y$is the cross-estuary wind stress, *a* and *b* are coefficients controlled by *f* and *K* (Appendix). The rotational solution introduces the impact from the cross-estuary winds. It also contains the non-rotational solution. For the Coupled case, u_w is 0.054 ms^{-1}; for the NARR case, u_w is 0.043 ms^{-1}. The results indicate northward cross-estuary wind enhances the surface down-estuary flow. However, the increases of exchange flow for the windy cases relative to the No-Wind case are greater than 0.08 ms^{-1}. This implies pure barotropic wind-driven circulation is only part of the mechanism for the exchange flow enhancement. Thus, the winds also indirectly affect the exchange flow in CLIS.

The Wedderburn number evaluates the ratio of wind stress to the aligned baroclinic pressure gradient (Monismith, 1986; Chen & Sanford, 2009):

$$W = \frac{\tau_x L}{\Delta\rho g H^2} \quad (1)$$

where, *L* is the estuary length scale, $\Delta\rho$ is the horizontal density difference, and *g* is the gravitational acceleration. *W* is applied in the estuary's axial direction with along-estuary wind and density gradient, but it also can be applied in the lateral direction with cross-estuary wind and density gradient. Both the along- and cross-estuary *W* (Table 4) in CLIS during the early bottom intrusion period (20~25th tidal cycle) are estimated. For the Coupled case, the cross-estuary *W* is 0.46, which is larger than the along-estuary *W* (0.33). It suggests the cross-estuary winds play more important role than the along-estuary component at this time. While for the NARR case, the corresponding *W* numbers are 0.15 and 0.07. Both are smaller, and the down-estuary wind is relatively more important.

Scully et al. (2005) demonstrate mild down-estuary winds can increase vertical stratification and intensify the tidal averaged exchange flow. In their study wind straining is more important than wind mixing. Wilson et al. (2015) found summertime *W* in WLIS ranges from 0.75 to 2.5. Due to freshwater input from the East River, the longitudinal density gradient is five times the lateral one. They suggested wind straining play more role on density modification than mixing in WLIS. While the *W* values in this study are lower than theirs. However, the model results do not suggest much longitudinal straining caused by down-estuary fresher water delivery in CLIS.

Actually, the straining is more lateral. Though the down-estuary winds in NARR case are mild (<5 ms^{-1}), the wind mixing steepens the isopycnals at the northern upper layer of the section. This generates stronger lateral straining compared to the No-Wind case, and further intensifies the quasi-geostrophic exchange flow. Similar processes have been observed and simulated in the Chesapeake Bay (Guo & Valle-Levinson, 2008; Li & Li, 2011; Xie & Li, 2018).

Winds in the Coupled case are somewhat more energetic than the NARR one, with stronger northward winds. Greater wind mixing reduces the lateral straining. But the northward winds tilt the sea level upward from the middle section northward, which generates barotropic up-estuary components and thereby strengthens the total inflow. Few studies focus on the cross-estuary winds effects. Guo and Valle-Levinson (2008) examined impacts of wind direction variation on exchange flow in the Chesapeake Bay. Their model results show cross-estuary winds build up lateral sea level gradient and modify the exchange flow strength.

It also worthwhile to derive a new dimensionless number that rates the relative importance of barotropic wind effects in wide estuaries, with large Kelvin numbers. The axial Wedderburn number can be viewed as the ratio of along-estuary flows driven by along-estuary winds and along-estuary density gradients. Because both terms appear in the same momentum equation, it is sufficient to compare the along-estuary wind stress and baroclinic terms in *W*. The quasi-geostrophic dynamics likely in the cross-estuary direction of a wide estuary provide a scaling for the along-estuary flow in terms of the cross-estuary density gradient: $gH\Delta\rho/\rho Lf$, where $\Delta\rho$ and L are cross-estuary scales. The new dimensionless number (W_{geo}) is the ratio of the rotational u_w expression (given above) to the geostrophic scaling:

$$W_{geo} = \frac{(a\tau_x - b\tau_y)Lf}{gK\Delta\rho} \quad (2)$$

This number compares the along-estuary flows generated by the barotropic response to the wind stress and the geostrophic response to the cross-estuary density gradient. W_{geo} is 1 for the Coupled case, suggesting the barotropic response to winds is significant, as strong as the density-driven flow. It is worth to note that both the density-driven and wind-driven flows are parts of the along-estuary exchange flow; horizontal advection also has influence. W_{geo} for the NARR case is 0.26, indicating weaker barotropic wind influence for this case. This dimensionless number is applicable to other wide estuaries.

Overall, the stronger Coupled winds have a greater role on directly enhancing the exchange flow, and the cross-estuary wind has more contribution on that. While the NARR winds have impacts on exchange flow more indirectly through modification of the density field.

4.4 Wind resolution to surface drifter track simulation

Intercomparison of model cases indicate wind is a necessary forcing to simulate reasonable drifter tracks. Further move, surface drifter tracks (and other surface particle paths) are among the hydrodynamic features the most sensitive to winds, with large differences resulting from even mild winds. Higher resolution wind forcing, such as the Coupled WRF winds, can better represent the drifter distribution. Nevertheless, there are mismatches still to be improved. Similar comparisons in a tidal inlet (Spydell et al., 2015) show lower simulated drifter speeds and differences on distribution directions to observations. Besides wind impacts, many other factors (e.g. model resolution, bathymetry) can influence the results. A robust comparison of observed and modeled drifter paths would require many more field releases.

4.5 Is coupling necessary?

Though WRF winds help on drifter simulations and result in some differences (relative to the NARR forcing) in the estuary and on the shelf, the coupling is computationally expensive. For this study computation time is ten times longer with coupling. On the other hand, both the Coupled and NARR cases offer similar strength of estuarine exchange flow and dye pulse transport in CLIS. That suggests the NARR forcing is sufficient for long-term spin-up and studying seasonal scale processes. While coupling with WRF offers benefits for shorter term simulations focusing on smaller scale features. Both methods perform reasonably well during summertime LIS conditions. Thus, coupling with an atmospheric model has benefits, but is not absolutely necessary to represent many of the main features of this large estuary-shelf system.

5 Conclusions

Summertime low discharge Connecticut River water pathways are detected by running simulations with a passive dye pulse and surface drifters. Entering at the northern coast near the sound mouth, the special geological position of the river mouth causes its water to have two main pathways. Both interact with the two-layer estuarine circulation. By the end of the 19-day analysis period, the near-bottom up-estuary pathway slowly moves a third of the river water westward with the denser estuarine inflow. This pathway is controlled by the spring-neap tides over the Mattituck Sill. The surface down-estuary pathway quickly transports a third of the river water onto the shelf. And this pathway is confirmed by both satellite-tracked and numerical surface drifters. The remaining third is still in ELIS at the end of the analysis period.

Three scenarios of wind forcing are tested: The Coupled case with high spatially varied WRF winds, the No-Wind case with no wind stress, and the NARR case with relatively spatial uniform winds. Comparisons with the No-Wind case show the wind is a necessary ingredient. Inside LIS, without wind forcing, the strength of the exchange flow is reduced and the timing of the river water up-estuary transport is delayed. On the shelf, shutting down the wind significantly reduces the cross-shelf transport of the fresher estuarine outflow, including the Connecticut River water. However, the Wedderburn number and a new analogous dimensionless number (W_{geo}) appropriate for wide estuaries with a quasi-geostrophic cross-estuary balance suggest the mild summer winds impacts are secondary in LIS. The mild down-estuary NARR winds cause lateral staining, which alters the position and enhances the strength of the exchange flow in CLIS. Although the slightly energetic WRF winds weaken the lateral staining, the additional northern cross-estuary winds strengthen the exchange flow. Despite the corresponding W_{geo} suggests wind-driven flow has similar strength to the density-driven one, the horizontal advection also has

strong impacts. Both the lateral staining and cross-estuary winds-driven exchange flow enhancement mechanisms can be applied to other wide estuaries.

The Coupled and NARR cases display similar level of performance on simulating estuarine exchange flow and the river water dye transport in LIS. But the model is more sensitive to different wind forcing on the shelf where the tidal impacts decrease. Although it is computationally expensive, the results suggest a fully coupled atmosphere-ocean model, instead of low resolution NARR forcing, offers better spatial variations on modeling drifter tracks and some differences in freshwater patterns in the estuary and shelf. Thus, coupling in this case provides advantages, but it does not fundamentally change the main features of the model solution.

Acknowledgements

This study was supported by NSF Grant 0955967 (Physical Oceanography), NASA Grant NNX13AE25G, and UCONN Marine Sciences predoctoral summer funding 2013. Simulations were run with high-performance computing support from Yellowstone (ark:/85065/d7wd3xhc) provided by NCAR's Computational and Information Systems Laboratory, sponsored by the National Science Foundation. The observational study was helped considerably by Turner Cabaniss at UCONN Marine Sciences. This manuscript was improved by helpful suggestions of anonymous peer reviewers and the editor.

Appendix

Winant (2004) described the rotational solution of the wind-driven flow in an elongated basin. The dimensionless 3D current, which is scaled by $\frac{|\tau|H}{\rho K}$, is

$$V = t_s \frac{\sinh[\alpha(z+h)]}{\alpha \cosh(\alpha h)} - \frac{N}{\alpha^2}\left[1 - \frac{\cosh(\alpha z)}{\cosh(\alpha h)}\right] \quad \text{(A1)},$$

where $t_s = t_s^x + it_s^y$ is the direction of the wind stress, $\alpha = \sqrt{\frac{ifH^2}{K}}$, H is the maximum depth, N is sea level gradient, and h is normalized water depth.

The vertically integrated transport is $\int_{-h}^{0} Vdz = t_s h^2 \frac{\cosh(\alpha h)-1}{(\alpha h)^2 \cosh(\alpha h)} + Nh^3 \frac{\tanh(\alpha h)-\alpha h}{(\alpha h)^3}$ (A2)

If the cross-estuary section is rectangular, water depth is constant ($h = 1$). For steady-state, $\int_{-h}^{0} Vdz = 0$ holds everywhere along the cross section, giving

$$N = -t_s \alpha \frac{\cosh(\alpha h)-1}{\cosh(\alpha h)} \frac{1}{\tanh(\alpha h)-\alpha h}.$$

Eliminating N in (A1), gives

$$V = t_s \left\{\frac{\sinh[\alpha(z+h)]}{\alpha \cosh(\alpha h)} + \frac{1}{\alpha} \frac{1}{\tanh(\alpha h)-\alpha h}\left[1 - \frac{1}{\cosh(\alpha h)}\right]\left[1 - \frac{\cosh(\alpha z)}{\cosh(\alpha h)}\right]\right\} \quad \text{(A3)}$$

Then, the dimensional surface wind driven velocity is

$$u_w + iv_w = \frac{(\tau_x + i\tau_y)H}{\rho K}\left\{\frac{\sinh[\alpha]}{\alpha \cosh(\alpha)} + \frac{1}{\alpha} \frac{1}{\tanh(\alpha)-\alpha}\left[1 - \frac{1}{\cosh(\alpha)}\right]^2\right\} \quad \text{(A4)}$$

For the along-estuary flow $u_w = \frac{(a\tau_x - b\tau_y)H}{\rho K}$, where $a + bi = \left\{\frac{\sinh[\alpha]}{\alpha\cosh(\alpha)} + \frac{1}{\alpha}\frac{1}{\tanh(\alpha)-\alpha}\left[1 - \frac{1}{\cosh(\alpha)}\right]^2\right\}$. If f=10^{-4} s^{-1}, H is 28 m, for the Coupled and NARR cases, K are 0.006 m^2s^{-1} and 0.004 m^2s^{-1}, respectively. The corresponding a+bi is 0.20-0.08i and 0.17-0.09i. The solution still holds for non-rotational condition, which gives a=0.25 and b=0.

References

Bennett, D. C., O'Donnell, J., Bohlen, W. F., & Houk A. (2010). Tides and overtides in Long Island Sound, *Journal of Marine Research*, **68**, 1-36. doi.org/10.1357/002224010793079031.

Chapman, D. C. (1985). Numerical treatment of cross-shelf open boundaries in a barotropic coastal ocean model. *Journal of Physical Oceanography*, **15,** 1060-1075.

Chen, S.-N., & Sanford, L. P. (2009). Axial wind effects on stratification and longitudinal salt transport in an idealized, partially mixed estuary. *Journal of Physical Oceanography*, **39,** 1905-1920. doi.org/10.1175/2009JPO4016.1.

Codiga, D. L., & Aurin, D. A. (2007). Residual circulation in eastern Long Island Sound: observed transverse-vertical structure and exchange transport. *Continental Shelf Research*, **27,** 103-116. doi.org/10.1016/j.csr.2006.09.001.

Csanady, G. T. (1973). Wind-induced barotropic motions in long lakes. *Journal of Physical Oceanography*, **3,** 429-438.

Cucco, A., Quattrocchi, G., Satta, A. Antognarelli, F. De Biasio, F., Cadau, E., Umgiesser, G., & Zecchetto, S. (2016). Predictability of wind-induced sea surface transport in coastal areas. *Journal of Geophysical Research*, **121,** 5847-5871. doi.org/10.1002/2016JC011643.

Egbert, G. D. & Erofeeva, S. Y. (2002). Efficient inverse modeling of barotropic ocean tides. *Journal of Atmospheric and Oceanic Technology*, **19**(2), 183-204.

Fairall, C. W., Bradley, E. F., Hare, J. E., Grachev, A. A., & Edson, J. B. (2003). Bulk parameterization of air-sea fluxes: Updates and verification for the COARE algorithm. *Journal of Climate*, **16,** 571-591.

Flather, R. A. (1976). A tidal model of the northwest European continental shelf. *Memoires de la Societe Royale de Sciences de Liege*, **10**(6), 141-164.

Garvine, R. W. (1974). Physical features of the Connecticut River outflow during high discharge. *Journal of Geophysical Research*, **79,** 831-846. doi.org/10.1029/JC079i006p00831.

Garvine, R. W. (1975). The distribution of salinity and temperature in the Connecticut River estuary. *Journal of Geophysical Research*, **80,** 1176-1183. doi.org/10.1029/JC080i009p01176.

Garvine, R. W. (1995). A dynamical system for classifying buoyant coastal discharges. *Continental Shelf Research*, **15,** 1585-1596. doi.org/10.1016/0278-4343(94)00065-U.

Geyer, W. R., & MacCready, P. (2014). The estuarine circulation, *Annual Review of Fluid Mechanics*, **46**, 175-197. doi.org/10.1146/annurev-fluid-010313-141302.

Goodrich, D. M., Boicourt, W. C., Hamilton, P., & Pritchard, D. W. (1987). Wind-induced destratification in Chesapeake Bay. *Journal of Physical Oceanography*, **17,** 2232-2240.

Gordon, R. B., & Pilbeam, C. C. (1975). Circulation in central Long Island Sound. *Journal of Geophysical Research*, **80,** 414-422. doi.org/10.1029/JC080i003p00414.

Gross, M. G., & Bumpus, D. F. (1972). Residual drift of near-bottom waters in Long Island Sound, 1969, *Limnology and Oceanography*, **17**, 636-638. doi.org/10.4319/lo.1972.17.4.0636.

Guo, X, & Valle-Levinson, A. (2008). Wind effects on the lateral structure of density-driven circulation in Chesapeake Bay. *Continental Shelf Research*, **28,** 2450-2471. doi.org/10.1016/j.csr.2008.06.008.

Haidvogel, D. B., Arango, H. G., Hedstrom, K., Beckmann, A., Malanotte-Rizzoli, P., & Shchepetkin, A. F. (2000). Model evaluation experiments in the North Atlantic Basin: Simulations in nonlinear terrain-following coordinates. *Dynamics of Atmospheres and Oceans*, **32**, 239-281. doi.org/10.1016/S0377-0265(00)00049-X.

Koppelman, L. E., Weyl, P. K., Gross, M. G., & Davies, D. S. (1976). *The urban sea: Long Island Sound*. New York, NY: Praeger Publishers.

Li, M., Zhong, L., Boicourt, W. C., Zhang, S., & Zhang, D.-L. (2007). Hurricane-induced destratification and restratification in a partially-mixed estuary. *Journal of Marine Research*, **65**, 169-192. doi.org/10.1357/002224007780882550.

Li, Y., & Li, M. (2011). Effects of winds on stratification and circulation in a partially mixed estuary. *Journal of Geophysical Research*, **116**, C12012. doi.org/10.1029/2010JC006893.

Liu, Q., Rothstein, L. M., & Luo, Y. (2017). A periodic freshwater patch detachment process from the Block Island Sound estuarine plume, *Journal of Geophysical Research*, **122**, 570-586. doi.org/10.1002/2015JC011546.

Lombardo, K., Sinsky, E., Jia, Y., Whitney, M. M., & Edson, J. (2016). Sensitivity of Simulated Sea Breezes to Initial Conditions in Complex Coastal Regions. *Monthly Weather Rev*iew, **144**, 1299-1320. doi.org/10.1175/MWR-D-15-0306.1.

Mesinger, F., DiMego, G., Kalnay, E., Mitchell, K., Shafran, P. C., Ebisuzaki, W., W., Jović, D., Woollen, J., Rogers, E., Berbery, E.H. & Ek, M.B. (2006). North American Regional Reanalysis. *Bulletin of the American Meteorological Society*, **87**, 343-360. doi.org/10.1175/BAMS-87-3-343.

Monismith, S. G. (1986). An experimental study of the upwelling response of stratified reservoirs to surface shear stress. *Journal of Fluid Mechanics*, **171**, 407-439. doi.org/10.1017/S0022112086001507.

O'Donnell, J., Dam, H. G., Bohlen, W. F., Fitzgerald, W., Gay, P. S., Houk, A. E., Cohen, D. C., & Howard-strobel, M. M. (2008). Intermittent ventilation in the hypoxic zone of western Long Island Sound during the summer of 2004. *Journal of Geophysical Research*, **113**, C09025. doi.org/10.1029/2007JC004716.

Orlanski, I. (1976). A simple boundary condition for unbounded hyperbolic flows. *Journal of Computational Science*, **21**(3), 251-269. doi.org/10.1016/0021-9991(76)90023-1.

Paskausky, D. F., & Murphy, D. L. (1976). Seasonal variation of residual drift in Long Island Sound. *Estuarine, Coastal Marine Science*, **4**, 513-522. http://doi.org/10.1016/0302-3524(76)90026-8.

667 Paskausky, D. F. (1977). Net drift in an atypical estuary, Long Island Sound. *Environmental*
668 *Management*, **1**, 331-342. doi.org/10.1007/BF01865860.

669 Scully, M. E., Friedrichs, C., & Brubaker, J. (2005). Control of estuarine stratification and
670 mixing by wind-induced straining of the estuarine density field. *Estuaries*, **28,** 321-326.
671 doi.org/10.1007/BF02693915.

672 Scully, M. E. (2010). Wind modulation of dissolved oxygen in Chesapeake Bay. *Estuaries and*
673 *Coasts*, **33**, 1164-1175. doi.org/10.1007/s12237-010-9319-9.

674 Signell, R. P., List, J. H., & Farris, A. S. (2000). Bottom currents and sediment transport in Long
675 Island Sound: A modeling study. *Journal of Coastal Research*, **16**(3), 551-566.

676 Sinsky, E. Z. (2016). *The impacts of surface conditions on sea breezes over coastal Connecticut*,
677 (Mater's theses). http://digitalcommons.uconn.edu/gs_theses/906 Storrs, CT: University of
678 Connecticut.

679 Spydell, M. S., Feddersen, F., Olabarrieta, M., Chen, J., Guza, R. T., Raubenheimer, B., & Elgar,
680 S. (2015). Observed and modeled drifters at a tidal inlet. *Journal of Geophysical Research*
681 *Oceans*, **120**, 4825-4844. doi.org/10.1002/2014JC010541.

682 Valle-Levinson, A., Reyes, C., & Sanay, R. (2003). Effects of bathymetry, friction, and rotation
683 on estuary–ocean exchange. *Journal of Physical Oceanography*, **33**(11), 2375-2393.

684 Valle-Levinson, A., & Wilson, R. E. (1994). Effects of sill processes and tidal forcing on
685 exchange in eastern Long Island Sound. *Journal of Geophysical Research*, **99**, C6, 12667-12681.
686 doi.org/10.1029/94JC00721.

687 Vieira, M. E. C. (2000). The long-term residual circulation in Long Island Sound. *Estuaries*, **23**,
688 199-207. doi.org/10.2307/1352827.

689 Warner, J.C., Sherwood, C.R., Signell, R.P., Harris, C., & Arango, H.G. (2008). Development of
690 a three-dimensional, regional, coupled wave, current, and sediment-transport model. *Computers*
691 *and Geosciences*, **34,** 1284-1306. doi.org/10.1016/j.cageo.2008.02.012.

692 Warner, J.C., Armstrong, B., He, R., & Zambon, J.B. (2010). Development of a Coupled Ocean-
693 Atmosphere-Wave-Sediment Transport (COAWST) modeling system. *Ocean Modeling*, **35,**
694 230-244. http://doi.org/10.1016/j.ocemod.2010.07.010.

695 Wong, K. C. (1991). The effect of East River on the barotropic motions in Long Island Sound,
696 *Journal of Marine Research*, **49**, 321-337. doi.org/10.1357/002224091784995873.

697 Whitney, M. M., & Codiga, D. L. (2011). Response of a large stratified estuary to wind events:
698 Observations, simulations, and theory for Long Island Sound. *Journal of Physical Oceanography*,
699 **41**, 1308-1327. doi.org/10.1175/2011JPO4552.1.

700 Whitney, M. M., Jia, Y., & McManus, P. M. (2014). Sill effects on physical dynamics in eastern
701 Long Island Sound. *Ocean Dynamics*, **64**, 443-458. doi.org/10.1007/s10236-013-0681-6.

702 Whitney, M. M., Ullman, D. S., & Codiga, D. L. (2016). Subtidal exchange in Eastern Long
703 Island Sound. *Journal of Physical Oceanography*, **46,** 2351-2371. doi.org/10.1175/JPO-D-15-
704 0107.1.

Wilkin, J. L., & Hunter, E. J. (2013). An assessment of the skill of real-time models of Mid-Atlantic Bight continental shelf circulation. *Journal of Geophysical Research Oceans*, **118**, 1-15, doi.org/10.1002/jgrc.20223.

Wilson, R. E., Bratton, S. D., Wang, J., & Colle, B. A. (2015). Evidence for directional wind response in controlling inter-annual variations in duration and areal extent of summertime hypoxia in western Long Island Sound. *Estuaries and Coasts*, **38**, 1735-1743. doi.org/10.1007/s12237-014-9914-2.

Winant, C. D. (2004). Three-dimensional wind-driven flow in an elongated, rotating basin. *Journal of Physical Oceanography*, **34,** 462-476.

Wu, H., & Zhu., J. (2010). Advection scheme with 3rd high-order spatial interpolation at the middle temporal level and its application to saltwater intrusion in the Changjiang Estuary. *Ocean Modeling*, **33**, 33-51. doi.org/10.1016/j.ocemod.2009.12.001.

Xie, X., & Li, M. (2018). Effects of wind straining on estuarine stratification: a combined observational and modeling study. *Journal of Geophysical Research: Ocean*. **123**, 2363-2380. doi.org/10.1002/2017JC013470.

Table 1. *Standard Deviation of Wind Stress, Surface (denoted by $_s$) and Bottom (denoted by $_b$) Salinity (S) and Tidal Averaged Velocity (U and V) Over the Modeling Period in Different Regions for the Coupled, No-Wind and NARR Cases.*

Regions	U-wind stress [Pa]	V-wind stress [Pa]	S_s	S_b	U_s [ms^{-1}]	V_s [ms^{-1}]	U_b [ms^{-1}]	V_b [ms^{-1}]
Coupled LIS	0.06	0.08	1.13	1.02	0.09	0.07	0.04	0.03
CoupledShelf	0.05	0.07	0.31	0.28	0.18	0.12	0.04	0.04
No-Wind LIS	0	0	1.19	1.02	0.08	0.07	0.03	0.03
No-Wind Shelf	0	0	0.38	0.28	0.12	0.12	0.03	0.04
NARR LIS	0.03	0.03	1.13	1.02	0.09	0.07	0.04	0.03
NARR Shelf	0.03	0.02	0.34	0.28	0.15	0.12	0.03	0.04

Table 2. *Root-Mean-Square Error (RMSE) and Its Percentage Relative to the Standard Deviation of the Coupled Case (in parentheses) of Wind Stresses, Surface (denoted by $_s$) and Bottom (denoted by $_b$) Salinity (S) and Velocity (U and V) Over the Modeling Period in Different Regions for the No-Wind and NARR Cases.*

Regions	U-wind stress [Pa]	V-wind stress [Pa]	S_s	S_b	U_s [ms^{-1}]	V_s [ms^{-1}]	U_b [ms^{-1}]	V_b [ms^{-1}]
LIS No-Wind	0.06 (100%)	0.08 (100%)	0.30 (27%)	0.19 (19%)	0.08 (89%)	0.07 (100%)	0.03 (75%)	0.02 (67%)
Shelf No-Wind	0.05 (100%)	0.07 (100%)	0.29 (94%)	0.16 (57%)	0.19 (105%)	0.10 (83%)	0.03 (75%)	0.03 (75%)
LIS NARR	0.04 (67%)	0.07 (88%)	0.21 (19%)	0.16 (16%)	0.05 (56%)	0.05 (71%)	0.02 (50%)	0.01 (33%)
Shelf NARR	0.03 (60%)	0.05 (72%)	0.18 (58%)	0.07 (25%)	0.10 (56%)	0.08 (67%)	0.02 (50%)	0.02 (50%)

Table 3. *Standard Deviation of U and V Winds from the Coupled (WRF) and NARR Cases and Buoy Observations in LIS.*

Wind Source	Temporal mean spatial variation U-wind [ms^{-1}]	Spatial mean temporal variation U-wind [ms^{-1}]	Temporal mean spatial variation V-wind [ms^{-1}]	Spatial mean temporal variation V-wind [ms^{-1}]
WRF	1.0	3.1	1.3	4.4
NARR	0.2	3.3	0.1	2.8
Buoy	1.3	2.9	1.2	3.4

730 **Table 4.** *Along- and Cross-Estuary Wind Stresses (τ), Density Difference (Δρ), Length Scale (L),*
731 *and Wedderburn Number (W) for the Coupled and NARR Cases.*

	Along-estuary				Cross-estuary			
	τ_x [Pa]	$\Delta\rho$ [kgm^{-3}]	L [km]	W	τ_y [Pa]	$\Delta\rho$ [kgm^{-3}]	L [km]	W
Coupled	0.03	0.6	40	0.26	0.07	0.2	10	0.46
NARR	0.02	0.7	40	0.15	0.03	0.6	10	0.07

732 **Figure 1**. Bathymetry of LIS region (colored). The grey contour is the 26-m isobath showing the
733 location of Mattituck Sill (M.S.). Magenta line is along-estuary section. Black lines are cross-
734 estuary sections. Sect-W and sect-C separate LIS into WLIS, CLIS, and ELIS. HU, HS, CT, and
735 TH denote Hudson, Housatonic, Connecticut, and Thames River, respectively. Magenta circle
736 demotes Fishers Island. Magenta cross marks the NOAA New London tidal station, which data is
737 used in Figure 2. Magenta triangles denote locations of four NOAA/UCONN buoys in LIS. The
738 inset (upper left plot) shows the three-layer WRF domain (white boxes) and ROMS domain
739 (green box) in the Coupled case.

740 **Figure 2**. From top to bottom, time series of water level from the Coupled case and the NOAA
741 New London station (Figure 1, magenta cross), Connecticut River daily discharge, with the river
742 dye pulse release period marked (blue bar), and U- and V-wind components from the Coupled
743 and NARR cases and buoys in LIS.

744 **Figure 3**. Coupled case salinity (colored) and velocity (black arrows) at surface (top) and bottom
745 (bottom). Results are averaged over the modeling period. The grey contour is the 26-m isobath.

746 **Figure 4**. M_2 tidal averaged plan view of water-column maximum dye concentration after 11, 19
747 and 36 tidal cycles for the Coupled, No-Wind, and NARR cases. The grey contour is the 26-m
748 isobath.

749 **Figure 5**. M_2 tidal averaged along-estuary section (Figure 1, thick red lines) view of dye
750 concentration (colored) and salinity (black contours, 0.5 intervals) after 11, 19 and 36 tidal cycle.
751 Mattituck Sill locates between station S4 and S5.

752 **Figure 6**. Time series of tidal averaged dye percentage in different regions (solid lines for the
753 total depth; dashed lines for 10 m below).

754 **Figure 7**. Observed surface drifter tracks and the corresponding model results for the Coupled,
755 NARR, and No-Wind cases. Dashed green and blue lines denote missing observational signals
756 on shelf.

757 **Figure 8**. Numbers (in $\log_2$ scale) of occurrences that drifters pass through a model grid cell.

758 **Figure 9**. Cross-estuary section (Figure 1, sect-C) view of along-estuary velocity u (colored,
759 positive down-estuary) and salinity (black contours, left column), total and baroclinic pressure
760 gradient terms in the cross-estuary direction (colored, right two columns), averaged over the 20th
761 ~ 25th M_2 tidal cycle.

762 **Figure 10.** Section-averaged momentum terms averaged over the 20-25 tidal cycles for the
763 Coupled, NARR, and No-Wind cases: hadv is horizontal advection, prs is the total PGF, bclc is
764 the baroclinic PGF, btp is the barotropic PGF, sstr is surface stress, bstr is bottom stress, and cor

765 is the Coriolis acceleration. Local acceleration is not shown since it is small. The u- and v-
766 momentum axes are aligned with the along- and cross-estuary directions.

Figure 1.

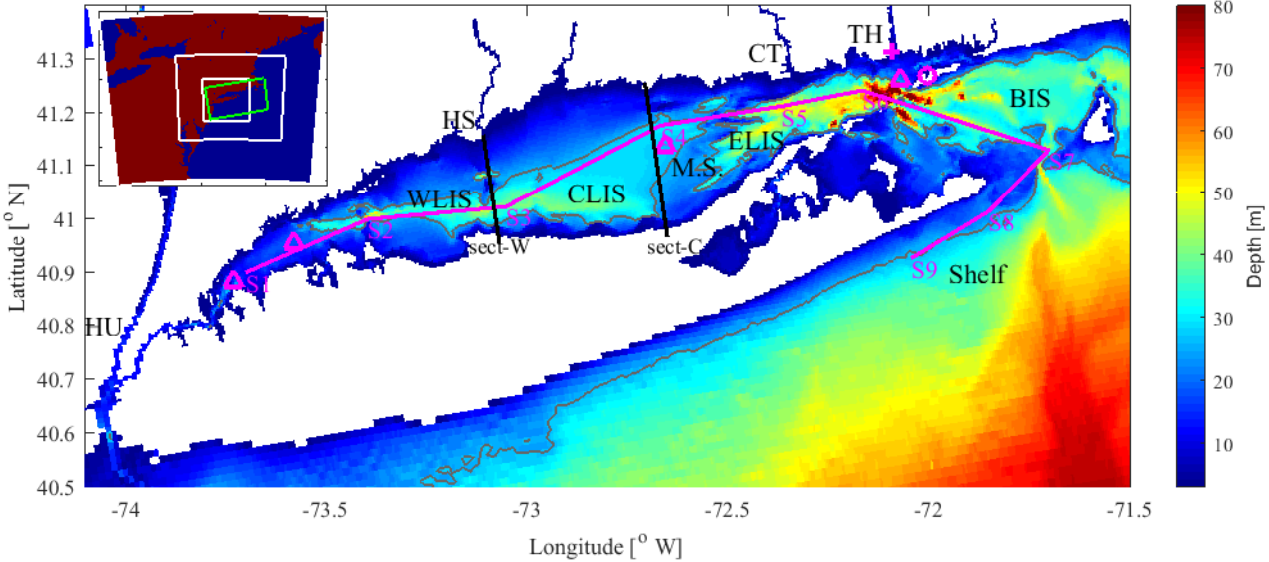
CT
TH
BIS
HS
ELIS
M.S.
WLIS
CLIS
sect-W
sect-C
S1
S2
S3
S4
S5
S6
S7
S8
S9
Shelf
HU
Latitude [° N]
Longitude [° W]
Depth [m]
41.3
41.2
41.1
41
40.9
40.8
40.7
40.6
40.5
-74
-73.5
-73
-72.5
-72
-71.5
80
70
60
50
40
30
20
10

Figure 2.

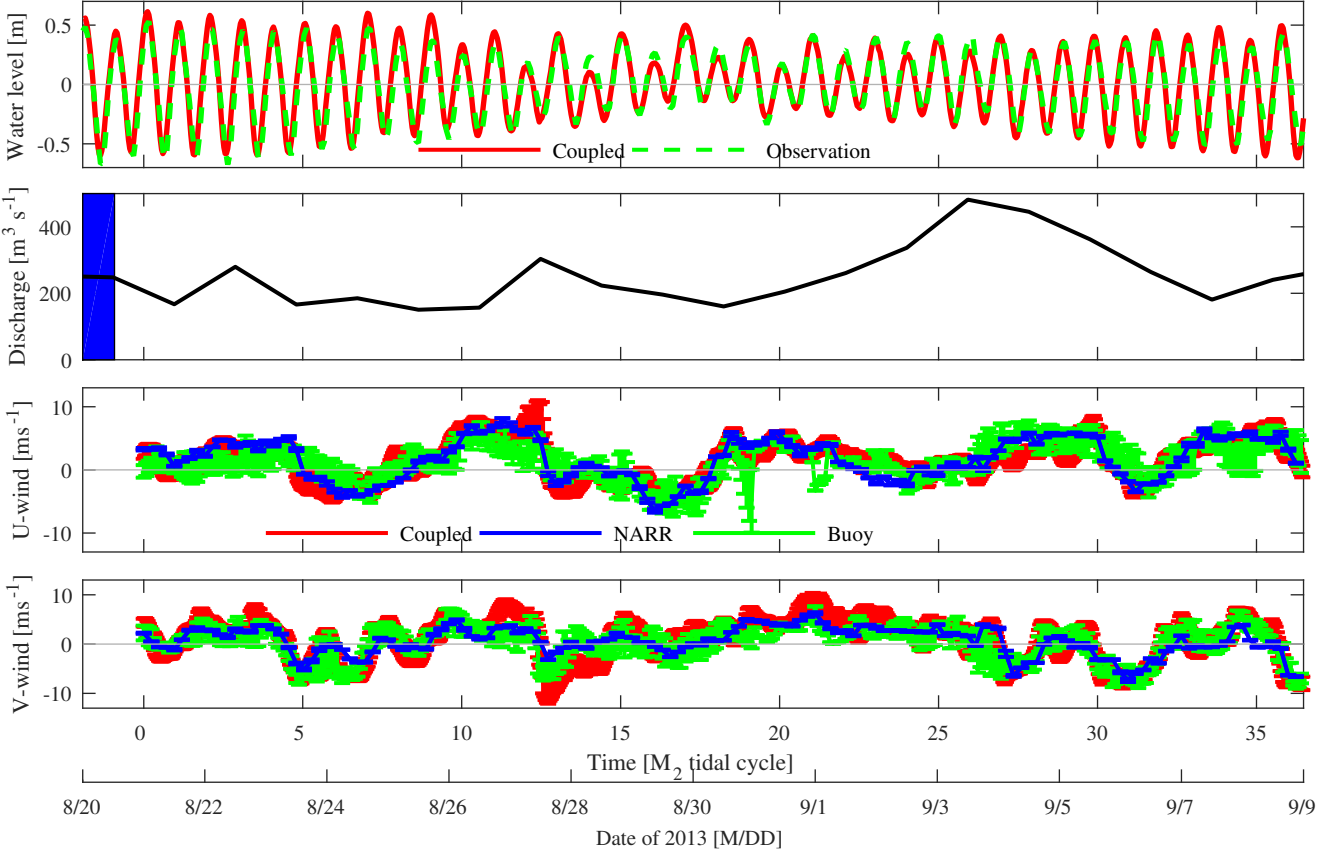
Water level [m]
0.5
0
-0.5
Coupled
Observation
Discharge [m^3 s^{-1}]
400
200
0
U-wind [ms^{-1}]
10
0
-10
Coupled
NARR
Buoy
V-wind [ms^{-1}]
10
0
-10
0
5
10
15
20
25
30
35
Time [M$_2$ tidal cycle]
8/20
8/22
8/24
8/26
8/28
8/30
9/1
9/3
9/5
9/7
9/9
Date of 2013 [M/DD]

Figure 3.

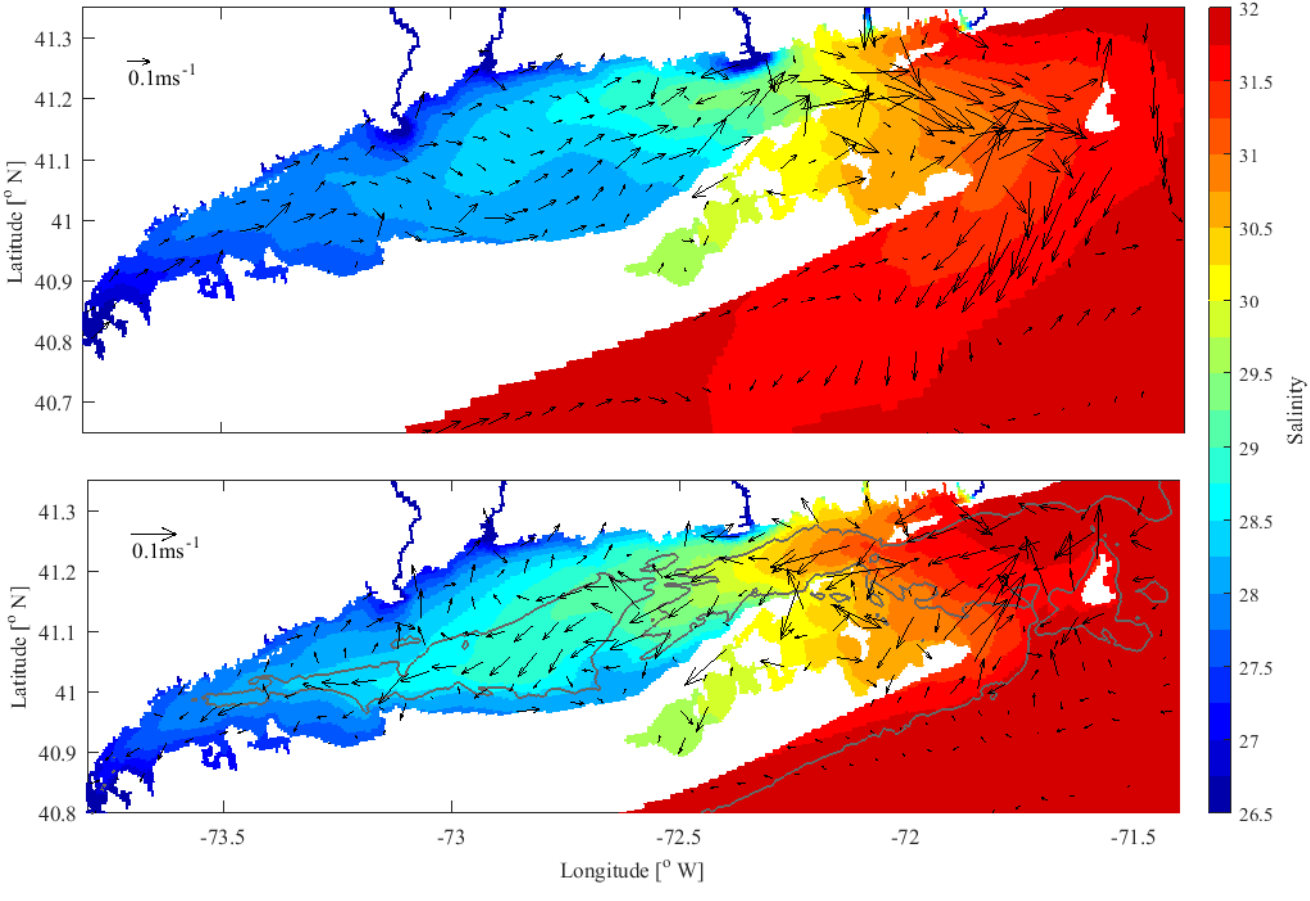
0.1ms-1
0.1ms-1
Latitude [° N]
Longitude [° W]
Salinity
41.3
41.2
41.1
41
40.9
40.8
40.7
-73.5
-73
-72.5
-72
-71.5
32
31.5
31
30.5
30
29.5
29
28.5
28
27.5
27
26.5

Figure 4.

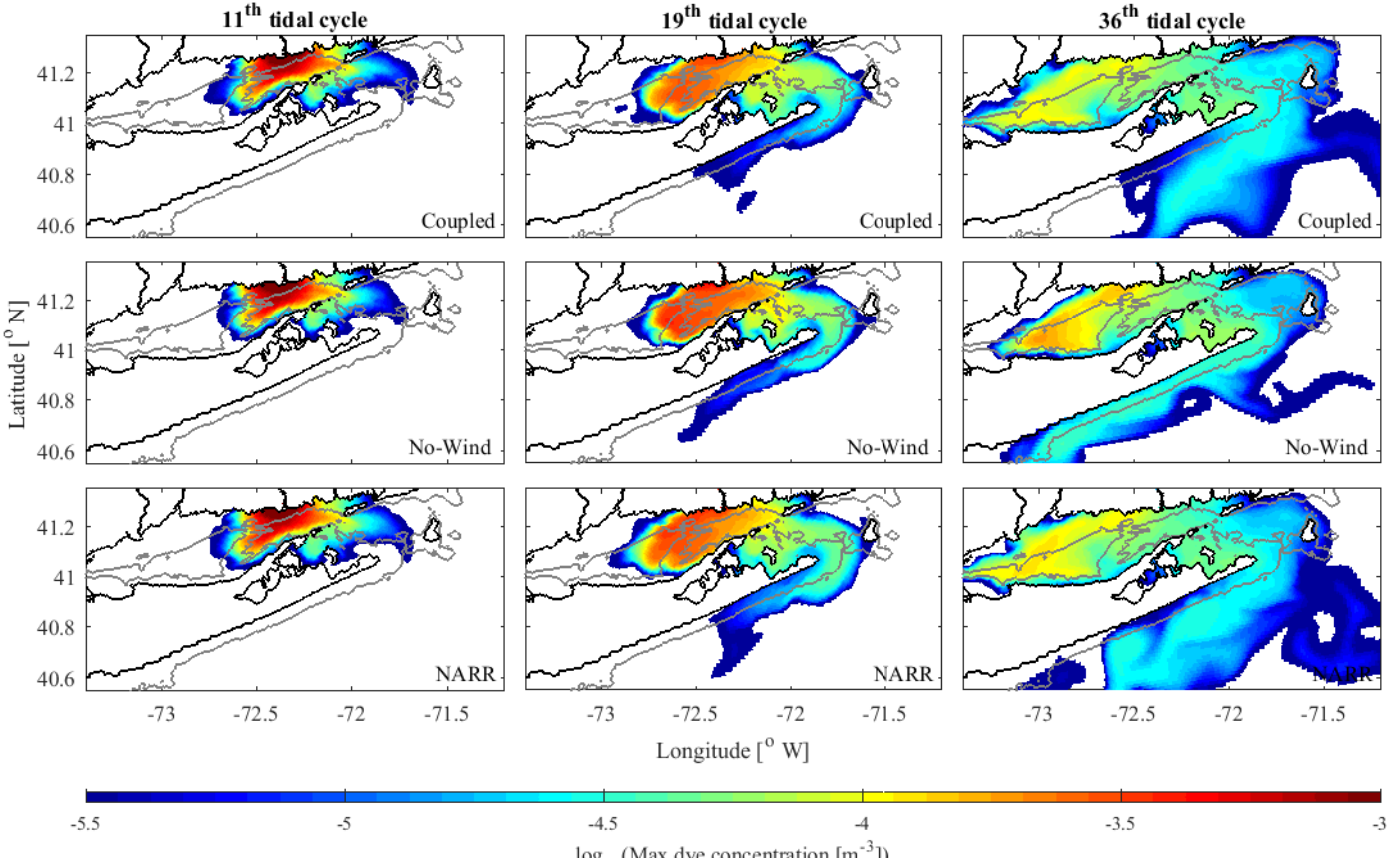
11th tidal cycle
19th tidal cycle
36th tidal cycle
Coupled
No-Wind
NARR
41.2
41
40.8
40.6
Latitude [° N]
-73
-72.5
-72
-71.5
Longitude [° W]
-5.5
-5
-4.5
-4
-3.5
-3
log10(Max dye concentration [m-3])

Figure 5.

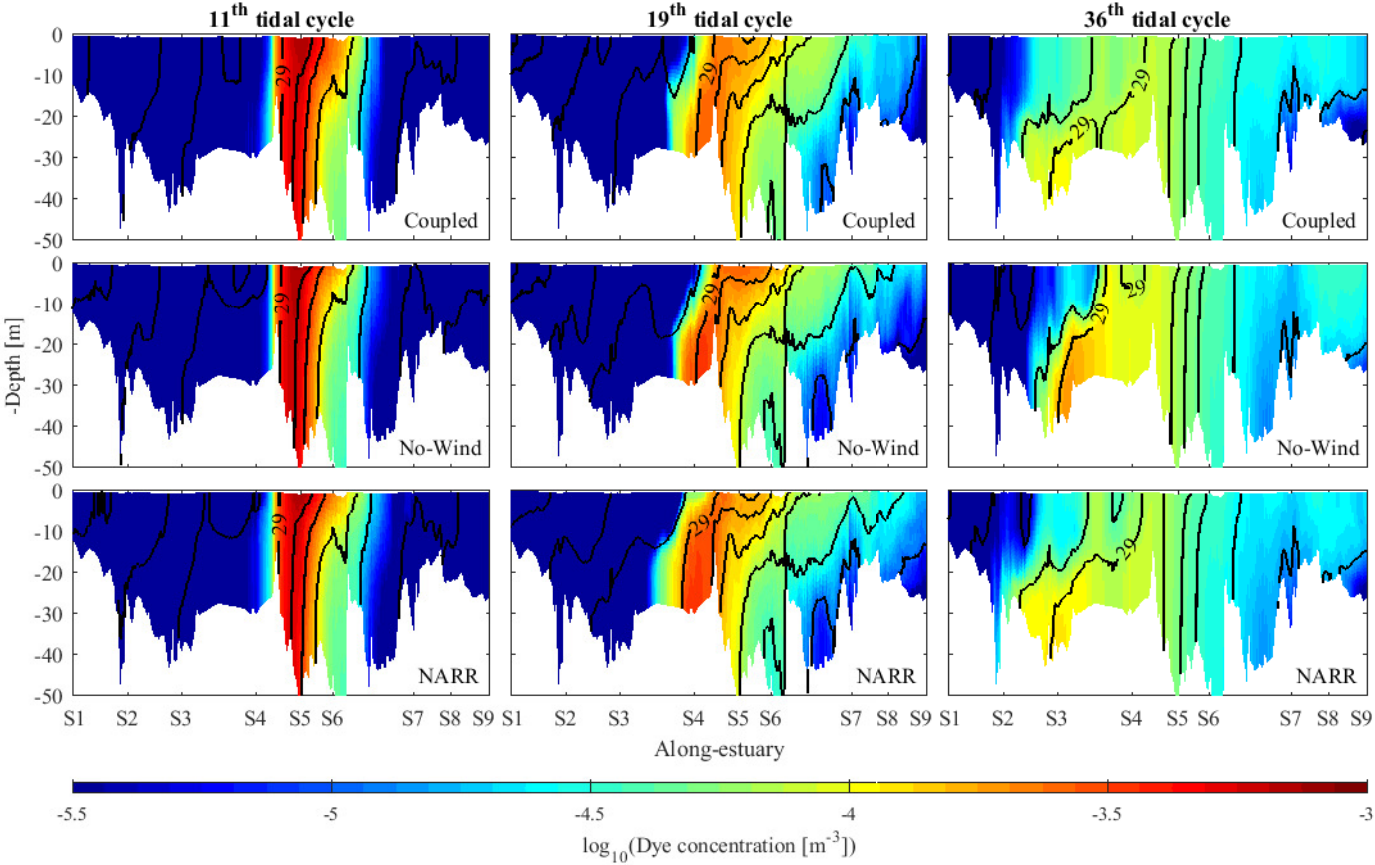
11th tidal cycle
19th tidal cycle
36th tidal cycle
Coupled
No-Wind
NARR
29
0
-10
-20
-30
-40
-50
-Depth [m]
S1
S2
S3
S4
S5
S6
S7
S8
S9
Along-estuary
-5.5
-5
-4.5
-4
-3.5
-3
log10(Dye concentration [m-3])

Figure 6.

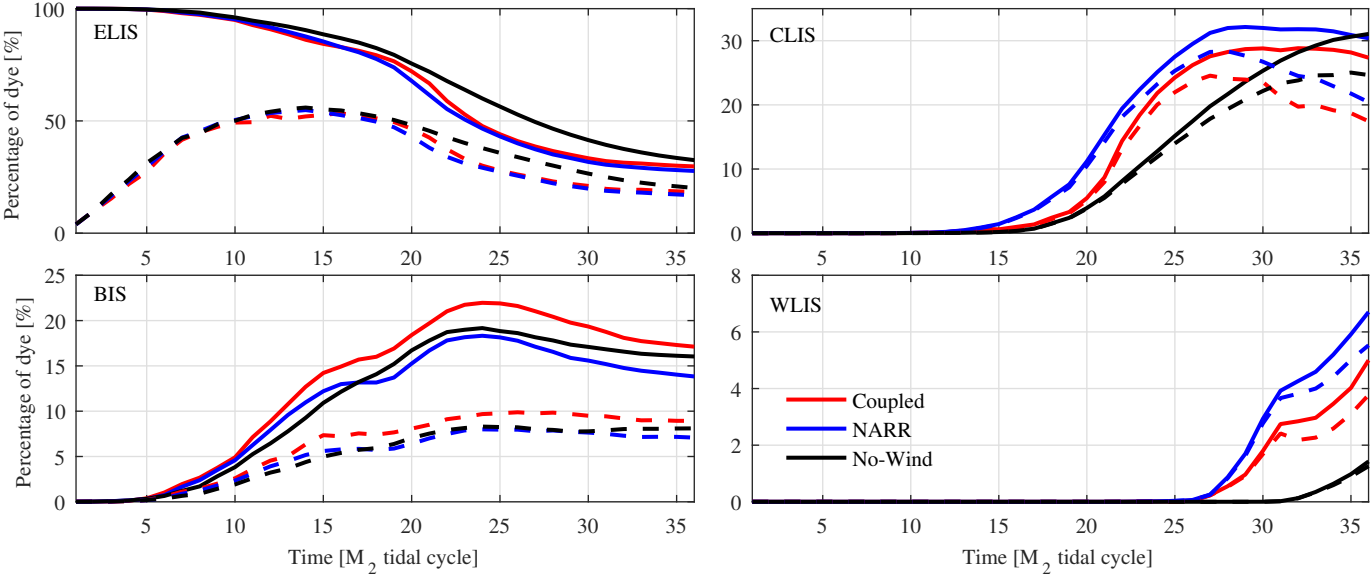
ELIS
CLIS
BIS
WLIS
Percentage of dye [%]
Percentage of dye [%]
Time [M 2 tidal cycle]
Time [M 2 tidal cycle]
Coupled
NARR
No-Wind

Figure 7.

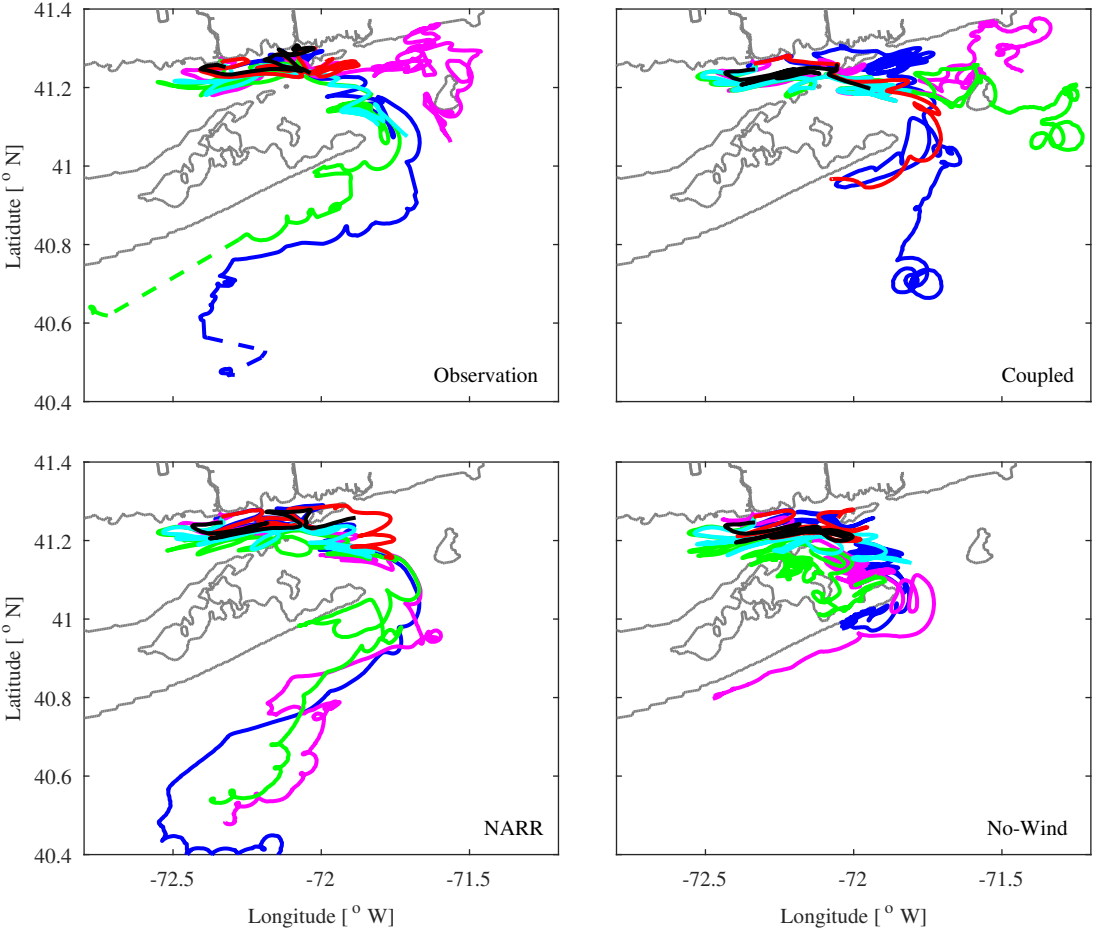
Latidute [o N]
41.4
41.2
41
40.8
40.6
40.4
Observation
Coupled
Latitude [o N]
NARR
No-Wind
-72.5
-72
-71.5
Longitude [o W]
Longitude [o W]

Figure 8.

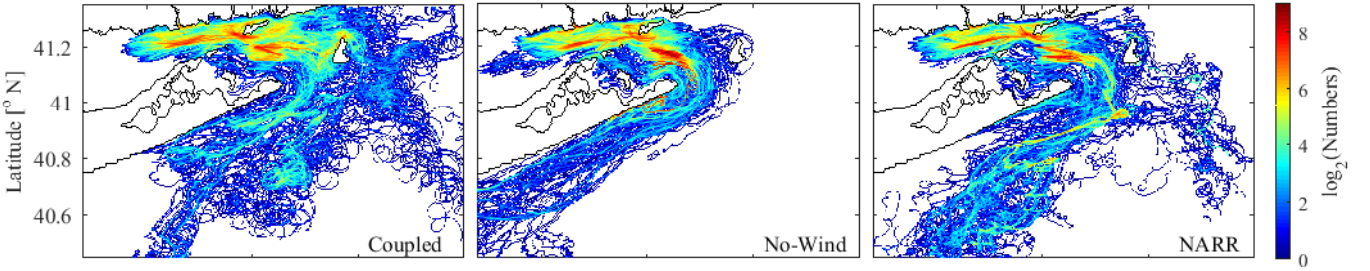
Latitude [° N]
41.2
41
40.8
40.6
Coupled
No-Wind
NARR
-72.5
-72
-71.5
-71
Longitude [° W]
log2(Numbers)
8
6
4
2
0

Figure 9.

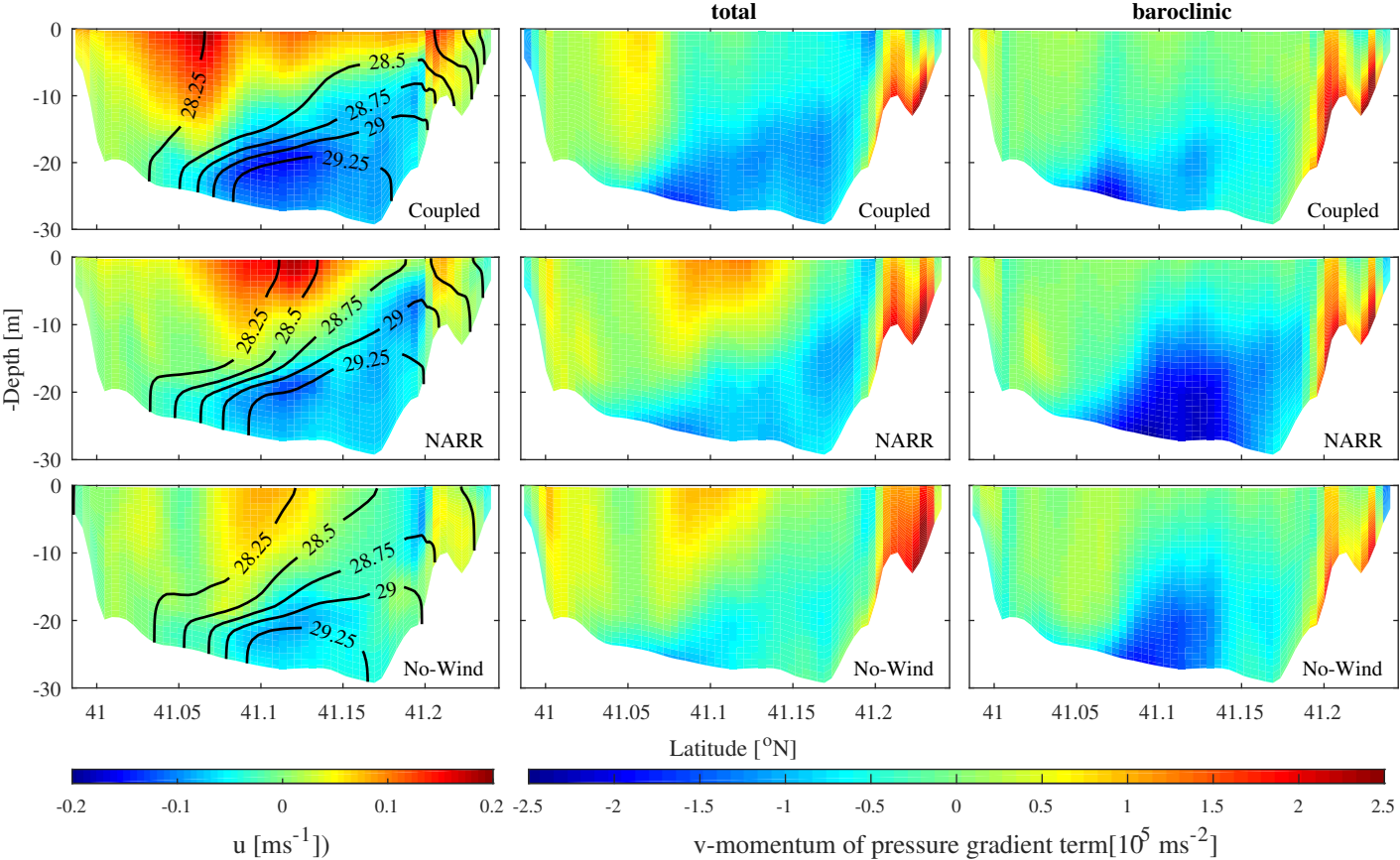
total
baroclinic
Coupled
NARR
No-Wind
28.25
28.5
28.75
29
29.25
-Depth [m]
0
-10
-20
-30
41
41.05
41.1
41.15
41.2
Latitude [°N]
-0.2
-0.1
0
0.1
0.2
u [ms-1])
-2.5
-2
-1.5
-1
-0.5
0
0.5
1
1.5
2
2.5
v-momentum of pressure gradient term[10^5 ms^-2]

Figure 10.

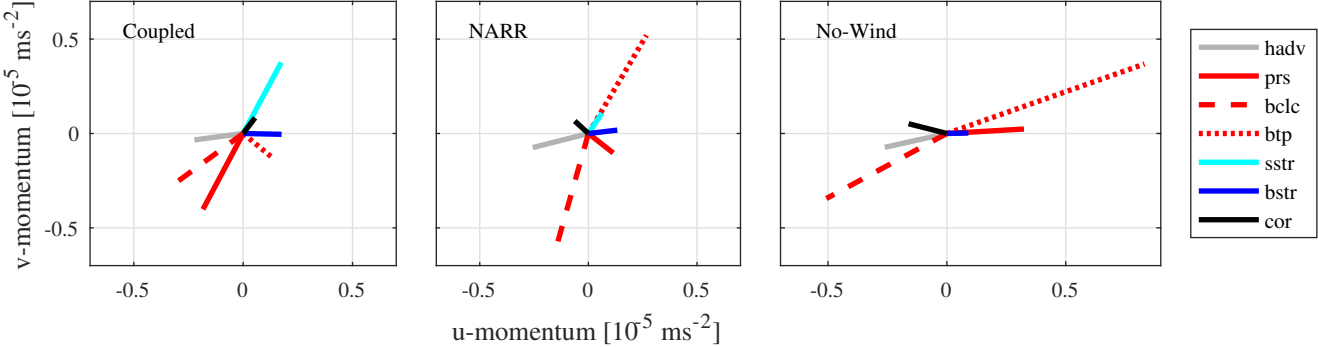
Coupled
NARR
No-Wind
v-momentum [10^-5 ms^-2]
u-momentum [10^-5 ms^-2]
0.5
0
-0.5
-0.5
0
0.5
hadv
prs
bclc
btp
sstr
bstr
cor